

Parametric Excitation and Instabilities of Spin Waves driven by Surface Acoustic Waves

Moritz Geilen,¹ Roman Verba,² Alexandra Nicoloiu,³ Daniele Narducci,^{4,5} Adrian Dinescu,³ Milan Ender,¹ Morteza Mohseni,¹ Florin Ciubotaru,⁴ Mathias Weiler,¹ Alexandru Müller,³ Burkard Hillebrands,¹ Christoph Adelmann,⁴ and Philipp Pirro¹

¹*Fachbereich Physik and Landesforschungszentrum OPTIMAS, Technische Universität Kaiserslautern, Germany**

²*Institute of Magnetism, Kyiv 03142, Ukraine*

³*National Institute for Research and Development in Microtechnologies, Bucharest R-07719, Romania*

⁴*imec, Leuven B-3001, Belgium*

⁵*KU Leuven, Departement Materiaalkunde, 3001 Leuven, Belgium*

(Dated: January 12, 2022)

The parametric excitation and instabilities of spin waves by short-waved coherent surface acoustic waves is demonstrated experimentally in metallic magnetic thin film structures. The magnon modes involved in the parametric processes are analyzed with micro-focused Brillouin light scattering. Complementary micromagnetic simulations combined with analytical modelling are used to determine the origin of the spin-wave instabilities. Depending on the experiment conditions, we observe a four-magnon instability of the magnon mode, linearly driven by the phonon, as well as a direct first-order parametric phonon-to-magnon instability, which is enhanced by a three-magnon splitting of the non-resonantly driven magnon, and even three-wave magnon and magnon-phonon confluence processes. Our results demonstrate that an efficient excitation of high amplitude, strongly nonlinear magnons in metallic ferromagnets is possible by surface acoustic waves and that parametric amplification of magnons by phonons can be realized. This opens novel ways to create micro-scaled nonlinear magnonic systems for logic and data processing which can profit from the high excitation efficiency of phonons using piezoelectric effects.

Magnetoelasticity, the interaction between magnetism and mechanical strain, is a promising mechanism towards compact, energy-efficient and even ultrafast spintronic devices. In particular, the influence of mechanical strain on spin waves, the fundamental excitations in a magnetic solid, is a crucial topic. Many studies have shown that a static strain generates a magneto-elastic field by the Villari effect, which can be used to manipulate the ferromagnetic resonance or the propagation of spin waves [1–4]. The interaction between dynamic strain, in the form of bulk acoustic waves (BAW) and spin waves and accordingly the formation of hybrid magneto-elastic waves has been studied extensively already in the 1950s and 1960s. As theoretically suggested by Kittel [5] the excitation of BAW by spin waves [6] and conversely the excitation of spin waves by BAW has been demonstrated [7]. In the linear regime of magneto-elastic coupling, it is proven that the frequency and momentum of the initial wave is transferred during the excitation. In the nonlinear regime, the parametric excitation of BAW has been shown in high-power ferromagnetic resonance experiments [8]. The parametric generation of spin waves by BAW, on the other hand, has been theoretically described and indirectly demonstrated by Morgenthaler [9] via the breakdown of the phonon pulses. Recently, the parametrically pumped magnons by BAWs have been directly measured by inductive microantennas [10] or the inverse spin Hall effect [11, 12].

In recent years, the focus in the field of dynamic magnetoelasticity has shifted towards coupling with surface acoustic waves (SAW) in hybrid magneto-elastic structures [13–15], since they offer a large variety of different modes leading to interesting coupling phenomena [16, 17]. In addition, their spatial localization to the surface makes their interaction with thin (magnetic) films placed on top of the wave-carrying sub-

strate much more efficient which opens various new opportunities for hybrid systems and devices [18, 19]. SAWs are nowadays used in many modern devices such as rf-filters, sensors or lab-on-a-chip applications [20, 21] due to their efficient and selective excitation on piezoelectric substrates accompanied with very low propagation losses. The excitation of spin waves by SAW and the associated effects on SAWs have been experimentally demonstrated in various magnetic materials [22–25]. These works represent a crucial step towards currentless spin-wave excitation, which is key to efficiently excite spin waves in magnonic circuits. Such magnonic circuits [26, 27] are considered a promising complementary technology to CMOS, since spin waves as information carriers do not suffer from the Joule losses that limit CMOS technologies and can be used for wave-based logic. Moreover, spin waves provide a broad spectrum of nonlinear phenomena [28–31], which opens the door towards novel applications like, e.g., neuromorphic computing [29, 32]. A crucial feature for neural networks is the presence of non-linear processes that start at a certain threshold. Nonlinear higher harmonic spin-wave generation induced by SAW has been shown in magnetic semiconductors [33]. However, parametric interaction between spin waves and SAW as predicted by theory [34, 35] has not been experimentally demonstrated.

In this letter, we present a study on spin-wave instabilities, in particular the parametric excitation of spin waves by short-waved, coherent SAWs in a thin metallic ferromagnetic film of CoFeB. Depending on the bias magnetic field, the magnetization dynamics is linearly or parametrically driven by the magneto-elastic field generated by SAWs. Micro-focused Brillouin light scattering spectroscopy (μ BLS, see Fig. 1) is used to study the different spin-wave modes in a frequency-resolved manner and to reveal the threshold behaviour of the

instability processes. Analytical modelling combined with full micromagnetic simulations is used to reveal the complex excitation schemes of the different instability processes by identifying the involved mechanisms and magnon modes (see Fig. 2). Depending on the experimental conditions, a four-magnon instability of the magnon mode, linearly driven by the phonon, is observed as well as a direct first-order parametric phonon-to-magnon instability, which is enhanced by three-magnon splitting of the non-resonantly driven magnon, and even three-wave magnon and magnon-phonon confluence processes.

In our experiment, an interdigital transducer (IDT) is used

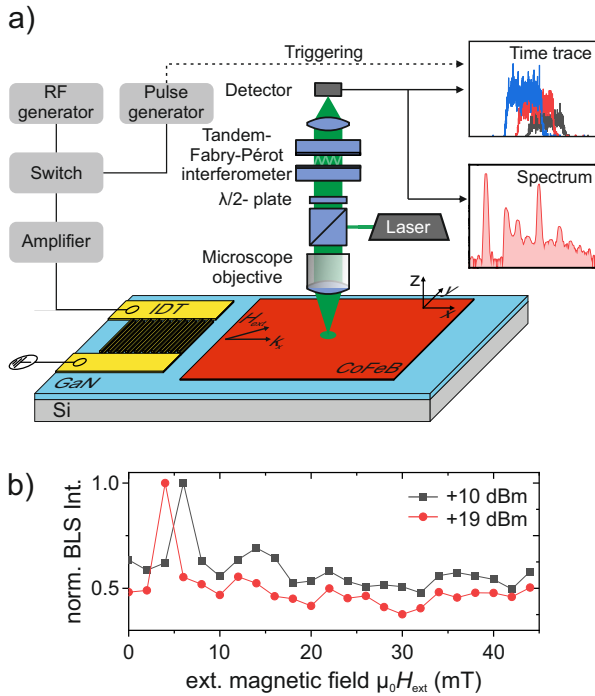


FIG. 1: a) Schematic illustration of the experimental setup. b) Normalized BLS intensity at the frequency of the fundamental mode $f_0 = 6.3$ GHz as a function of the applied magnetic field for linear and non-linear case. The maxima correspond to the resonant excitation of spin waves by the SAW.

to generate surface acoustic waves with a frequency $f_{\text{SAW}} = 6.31$ GHz and a wave vector $|k_{\text{SAW}}| = 9.2 \text{ rad}/\mu\text{m}$ in a $1.3 \mu\text{m}$ thick GaN layer on a silicon substrate. Details on the SAW excitation and propagation can be found in [36]. The spin waves are excited in a rectangular-shaped pad out of $h_{\text{CoFeB}} = 18 \text{ nm}$ thick $\text{Co}_{40}\text{Fe}_{40}\text{B}_{20}$ and are measured by μBLS [37–39]. An external magnetic bias field is applied in-plane with an angle of $\varphi = 45^\circ$ with respect to the propagation direction of the SAW (see Fig. 1 a). Since the excited Rayleigh mode only has strain components S_{ij} in the sagittal plane and the magnetization $\mathbf{M} = (M_x, M_y, M_z)$ is oriented in-plane, the magneto-

elastic field created by the SAW can be written as [40]:

$$\mu_0 \mathbf{H}_{\text{mel}} = -\frac{1}{M_S^2} \begin{pmatrix} 2B_1 S_{xx} M_x \\ 0 \\ B_2 S_{xz} M_x \end{pmatrix}. \quad (1)$$

Here, B_1 and B_2 are the magneto-elastic coupling constants of the CoFeB. In addition, near the surface, where the magnetic film is placed, it can be assumed that $|S_{xx}| \gg |S_{xz}|$.

Recently, we have characterized a similar structure in the linear excitation regime [39]. It was demonstrated that the resonant excitation of spin waves by the magneto-elastic field generated by the surface acoustic waves causes a strong increase in the spin-wave intensity at the resonance field as shown in Fig. 1 b). In this process, both the frequency and the wave vector of the SAW are transferred to the spin wave $(f_{\text{SAW}}, k_{\text{SAW}}) = (f_0, k_0)$. By increasing the RF power, this resonance condition is non-linearly shifted to higher fields, due to the nonlinear shift of spin-wave dispersion [31].

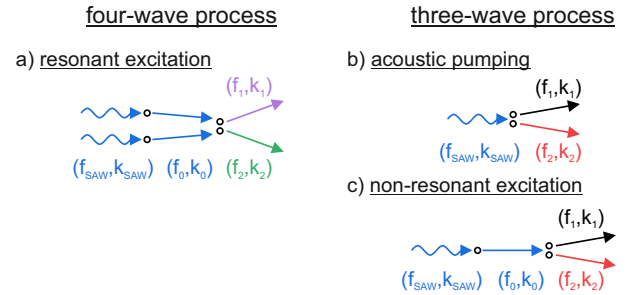


FIG. 2: Schematic illustration of the different instability processes with $(f_0, k_0) = (f_{\text{SAW}}, k_{\text{SAW}})$: four-wave-process: a) spin waves with (f_0, k_0) are resonantly excited by SAWs with $(f_{\text{SAW}}, k_{\text{SAW}})$ subsequently causing second order spin-wave instability. three-wave-process: b) direct SAW-spin wave process representing the acoustic parametric pumping of spin wave modes (f_1, k_1) and (f_2, k_2) by the SAW. c) Spin waves with (f_0, k_0) are non-resonantly excited by the SAW, subsequently causing first order spin-wave instability.

First, the case of resonant spin-wave excitation by the magneto-elastic field beyond the linear regime will be studied. The magnetic field is kept constant to $\mu_0 H_{\text{ext}} = 6 \text{ mT}$ and the BLS spectrum for magnons is measured as a function of the applied RF power (see Fig. 3 a). The power P applied to the IDT is varied between 0 dBm and +30 dBm. For low powers, only the directly excited mode f_0 is present. If the power is increased, a strong broadening of the initial mode and the appearance of two additional modes $f_1 = 5.7 \text{ GHz}$ and $f_2 = 6.9 \text{ GHz}$ can be observed close to f_0 . These two modes satisfy the energy conservation law $2f_0 = f_1 + f_2$ and, thus, can be attributed to a parametric instability of the second order [28]. For even higher excitation powers (see Fig. 3 b, blue line), spin waves are excited throughout a broad range of

the spin-wave band. These spin waves are caused by further, higher order scattering channels with higher thresholds. This region, which is referred to as supercritical regime [28, 30], will not be considered further. Instead, we will restrict ourselves to the region close to the threshold where only a single instability process occurs. A characteristic of nonlinear instability processes is a clear threshold in the initial spin-wave mode's amplitude. This threshold is determined by the minimum of the ratio between the effective relaxation frequency and the coupling strength between the involved magnon modes [31, 41, 42]. The BLS intensity of the three involved modes is presented in Fig. 3 c. The two secondary modes show a clear threshold behavior. Above their common threshold at +13dBm, the intensity of the modes increases abruptly and saturates quickly. The intensity of the initial mode, on the other hand, increases linearly up to this threshold value as illustrated by the dashed line in Fig. 3. Once the threshold is overcome and the scattering to the secondary modes occurs, the intensity of the initial mode starts to differ from this linear dependence and saturates for higher values, which is explained by the energy transfer to the secondary modes. It should be mentioned that the SAWs themselves can also exhibit nonlinear processes at sufficiently high amplitudes [43, 44]. These would also lead to a deviation from the linear behaviour, which is usually caused by the generation of higher harmonics, which, however, have not been observed in the experiment.

Thus, spin waves are resonantly excited by the SAWs, and subsequently undergo a four-magnon scattering process, leading to the second order spin-wave instability (see. Fig. 2 a). In principle, another four-wave process could be considered, in which two phonons split directly into two magnons. This process, however, is very unlikely since the Hamiltonian for such a process is described by $\mathcal{H} \sim q_k^2 c_{k_1}^* c_{k_2}^*$, where q_k and c_k are SAW and spin-wave amplitude. As the magneto-elastic energy is a linear function of the strain S , which is in turn proportional to q_k , this term is prohibited. Such process may only appear at very high SAW amplitude, at which the linear approximation of the strain ($S_{ij} = 1/2(\partial u_i/\partial x_j + \partial u_j/\partial x_i)$) becomes invalid.

After demonstrating the second order instability for a resonantly excited spin wave, we will now focus on a non-resonant case. The external magnetic field is, therefore, reduced to $\mu_0 H_{\text{ext}} = 2$ mT. As can be seen in Fig. 1 b the spin-wave intensity for the directly excited mode at f_0 is drastically reduced compared to the resonant case. However, instability processes can be observed in this case as shown in Fig. 4 a. In the linear regime, only a signal for the initial mode f_0 is present, which is non-resonantly driven by the SAW. At high powers four additional modes with different frequencies f_1 to f_4 are formed, which are symmetrically spaced around f_0 . Similar to the case of the second-order instability process, it can be stated that all four secondary modes show a common threshold value within the measurement accuracy. The initial mode starts to deviate from the

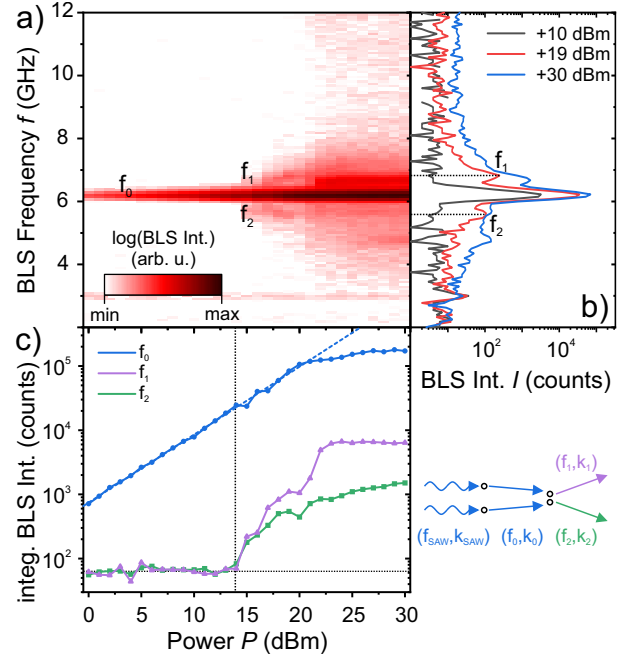


FIG. 3: Evolution of BLS spectra with an applied RF power a) and exemplary BLS spectra showing linear, critical and supercritical regimes b) at an external magnetic field of $\mu_0 H_{\text{ext}} = 6$ mT. c) Intensity for directly excited spin waves at $f_0 = 6.3$ GHz (blue) and the intensity of the secondary modes $f_1 = 6.9$ GHz (purple) and $f_2 = 5.7$ GHz (green). A linear progression is indicated by the blue dashed line and the threshold by the vertical black dotted line.

linear behaviour at this threshold value and begins to saturate (see Fig. 4 c). In the following, the origin of these secondary modes will be discussed. First, the two modes f_1 and f_2 with frequencies lower than f_0 are considered. Near the threshold (see Fig. 4 b), these modes have frequencies of $f_1 = 2.25$ GHz and $f_2 = 4.05$ GHz, which satisfy the conservation of energy for a three-wave process $f_0 = f_1 + f_2$ since they are equally spaced around half the frequency of the initial mode $f_0/2$. In materials with reciprocal dispersion relation, this asymmetric splitting is typically observed if the initial mode or driving field has a finite wave vector (another alternative is the splitting into different thickness modes, which does not apply in our case of sufficiently thin film).

In order to determine the wave vectors excited in the observed instability process, additional micromagnetic simulations were carried out using MuMax3 [45] and the software platform Aithericon [46]. The parameters used for the simulations can be found in the supplemental material [47]. The Rayleigh mode is implemented as plain waves of the strain components S_{xx} and S_{xz} [47]. We find that the magneto-elastic field non-resonantly drives the magnetization with the frequency and wave vector of the SAW $(f_{\text{SAW}}, k_{\text{SAW}}) = (f_0, k_0)$. The eigenstates for the specific frequencies are indicated by the isofrequency curves (dashed

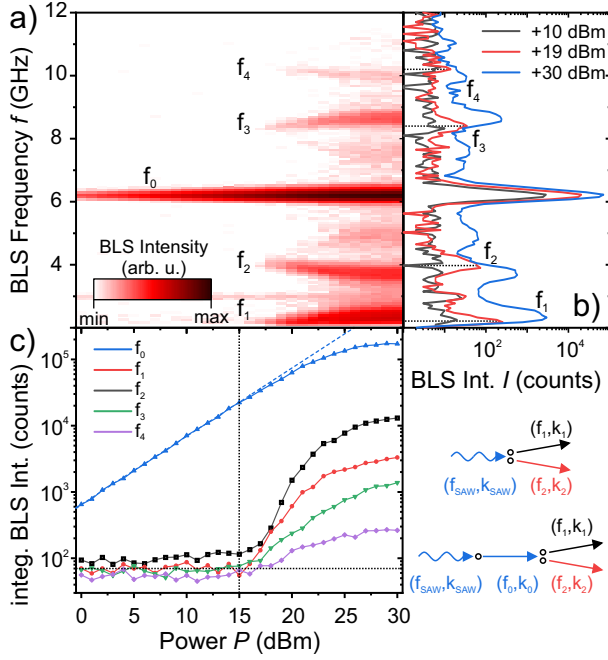


FIG. 4: a) Evolution of BLS spectra with an applied RF power a) and exemplary BLS spectra showing linear and critical regimes b) at an external magnetic field of $\mu_0 H_{\text{ext}} = 2 \text{ mT}$. c) Intensity at $f_0 = 6.3 \text{ GHz}$ (blue) and the intensity of the secondary modes f_1 (red), f_2 (black), f_3 (green) and f_4 (purple). A linear progression is indicated by the blue dashed line and the threshold by the vertical black dotted line.

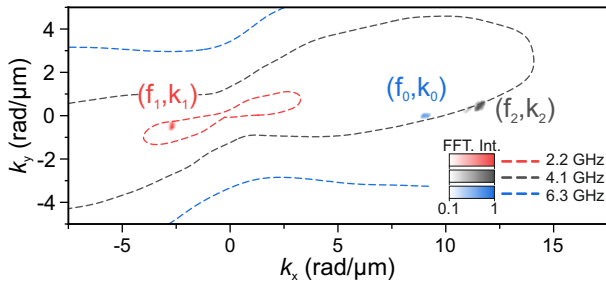


FIG. 5: Scheme of first order instability process. The magneto-elastic field is driven with $f_0 = 6.3 \text{ GHz}$ (blue) and leads to pumping of the spin-wave modes $f_1 = 2.2 \text{ GHz}$ (red) and $f_2 = 4.1 \text{ GHz}$ (black) while conserving momentum and energy.

lines). As can be seen in Fig. 5 (blue) this forced magnetization dynamics is not an eigenstate of the spin-wave system. Once the threshold is overcome, the onset of instability processes is observed. The two spin-wave modes with the lowest threshold, that can be observed in the simulation are: **1** with $(f_1 = 2.2 \text{ GHz}, \mathbf{k}_1 = (-2.5, -0.5) \text{ rad}/\mu\text{m})$ and **2** with $(f_2 = 4.1 \text{ GHz}, \mathbf{k}_2 = (11.6, 0.5) \text{ rad}/\mu\text{m})$. These spin-wave modes preserve, within the accuracy of the simulation, the wave vector of the pumping field, in order to fulfill momentum

conservation.

In principle, still two different three-wave processes are conceivable that cannot be distinguished based on the experimental observations: (i) the acoustic parametric pumping of two magnons by one SAW phonon (analogous to the parallel pumping of spin waves [48], see Fig.2 a) or (ii) the three-magnon splitting of spin waves, where in our particular case the excitations at f_0 are forced excitations by the SAW (see Fig.2 c). In order to determine which of the two processes is more efficient, the threshold value was theoretically determined for both. The acoustic pumping of spin waves by SAW is described by the following rate equation and a corresponding equation for c_2 [34]:

$$\frac{dc_1}{dt} + i\omega_1 c_1 + \Gamma_1 c_1 = i \mathcal{V}_{\text{SAW},12} q_{\text{SAW}} c_2^*, \quad (2)$$

where q_{SAW} relates to the SAW amplitude and c_i to the spin-wave amplitude of the i -th spin-wave mode. This process is resonant in \mathbf{k} fulfilling $k_{\text{SAW}} = k_1 + k_2$ and the parametric coupling efficiency is given by:

$$\mathcal{V}_{0,12} = \frac{\gamma B_1}{M_S} \bar{S}_{0,xx} [m_{1,x}^* m_{2,x}^* - \mathbf{m}_{1,x}^* \mathbf{m}_{2,x}^* \cos^2(\varphi_M)]. \quad (3)$$

Here $\mathbf{m}_{1,1}^*$ is the spin-wave mode structure and \bar{S} the averaged SAW strain in CoFeB layer. Details of the derivation can be found in supplementary material [47]. It is noteworthy that two contributions to the parametric coupling are present in Eq. 3. While the second one is proportional to the ellipticity of the magnetization trajectory, analogous to the pumping with electromagnetic waves, the first one is defined by the square of the dynamic magnetization components. This term is characteristic for anisotropy-type pumping, which is realized, e.g., for magneto-elastic [34] or magneto-electric [49] drives. The minimal threshold $q_{\text{th,min}}^{\text{SAW-SW}}$ is found for the splitting into magnons with $\mathbf{k}_1 = (8.1, -0.5) \text{ rad}/\mu\text{m}$, $\mathbf{k}_2 = (1.2, 0.5) \text{ rad}/\mu\text{m}$ and frequencies of 4.2 GHz and 2.1 GHz (see Fig. 6 diamonds). These predicted modes, however, are far apart in k -space from the modes predicted by the micromagnetic simulations (solid squares).

The second process that has to be considered is the SAW-driven first order instability, where forced excitations with $(f_{\text{SAW}}, k_{\text{SAW}})$ are excited. As for the previous process, a similar rate equation can be formulated to determine the threshold of the instability. For this purpose, the SAW amplitude q_{SAW} is replaced by the spin-wave amplitude of the non-resonant c_0 and the standard three-magnon scattering coefficient $V_{0,12}$ [31] is used as coupling parameter. The link between these q_{SAW} and c_0 can be found in the Supplement. It turns out that the minimum threshold for this instability process $q_{\text{th,min}}^{3\text{-magnon}}$ is about 64% larger than for the acoustic pumping process. However, although the first-order instability process does not occur, the three-magnon splitting takes place continuously. Thus it is necessary to take this energy flow into account when calculating the effective

damping of the secondary magnon modes for the acoustic pump process. The combination of these two mechanisms results in the threshold values shown in Fig. 5, where the modes with the lowest threshold value $q_{th,min}^{Comb}$ are marked with a star. These differ only slightly from the modes determined by the micromagnetic simulations. Moreover, the difference of the threshold values is less than 6%. As a result, even small differences in the modeling, i. e. the calculation of the demagnetization field, can explain this small discrepancy between analytical calculations and micromagnetic modelling. In summary, we find that the observed instability is

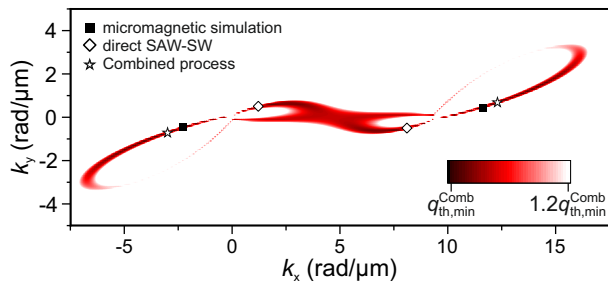


FIG. 6: Calculated threshold for the combined process of acoustic pumping process influenced by three-magnon scattering. The spin-wave modes with minimal threshold for the direct SAW-SW process $q_{th,min}^{SAW-SW}$ (diamond) and the combined process $q_{th,min}^{Comb}$ (star) are indicated. The modes extracted from the micromagnetic simulations are shown by the black squares.

caused by the acoustic pumping of magnons by the SAW phonons, which additionally benefits from the three-magnon scattering of magnons excited non-resonantly at the SAW frequency and wave vector (see Fig. 2). This process turns into a complex combined process of two coupled three-wave splitting processes especially at higher drives. Regarding the efficiency of the two processes, it remains to be mentioned that the linear excitation of spin wave at (f_0, k_0) is far from the resonance (2.3 GHz detuning) and, thus, SAW to spin wave conversion rate is low. The threshold of three-magnon splitting is, however, not far from that of the direct parametric SAW-to-SW process. It can be concluded that the latter can be observed only if linear SW excitation by SAW with subsequent three-magnon splitting is far from resonance or possesses symmetry restrictions.

From the positions of higher-frequency modes **3** and **4** one can imagine two possible mechanisms leading to their appearance. Either these are generated due to a three-wave confluence process ($f_0 + f_1 = f_3$ and $f_0 + f_2 = f_4$) or due to a parametric four-wave splitting process ($2f_0 = f_1 + f_4$ and $2f_0 = f_2 + f_3$). Calculations made using the Hamiltonian formalism (see Supplement [47]) show that in all the studied range (one order of magnitude above the threshold of the pumping process) the four-magnon process is two orders of magnitude weaker than dominating the three-magnon

one. The SAW-SW confluence process is two times more efficient than three-magnon confluence process, but, since the confluence process is non-threshold, both these processes contribute to the appearance of signals at $f_{3,4}$.

In summary, in this letter we have studied spin-wave instabilities driven by the magneto-elastic field generated by SAWs. We have investigated two different situations. In the resonant case, where spin waves are excited with the wave vector and the frequency of the SAW, the second-order instability process due to four-magnon scattering was observed above a certain SAW amplitude threshold. The second case was the non-resonant excitation of the magnetic system by the SAW. Here, we observed a complex combination of scattering processes, which were identified by a combined study of micromagnetic simulations and analytical modelling. The dominant process is the acoustic parametric pumping of magnons by the SAWs, which is enhanced by three-magnon scattering from the forced excitation at the SAW frequency. This contribution of the three-magnon process is crucial for the determination of the secondary modes. It should be emphasized that in contrast to the case of adiabatic parallel pumping, the initial nonzero wave vector of the SAW leads to a frequency non-degenerate splitting of the secondary modes. This provides an efficient control of the wave vector spectrum of pumped magnons.

To conclude, we have demonstrated that SAW-driven magneto-elastic interaction is sufficiently efficient and large enough to observe various nonlinear magnon and magnon-phonon phenomena, which are pre-requisites for magnon information processing systems. Thus, our work is a step toward efficient hybrid magnon-phonon systems.

Financial support by the EU Horizon 2020 research and innovation program within the CHIRON project (contract no. 801055) is gratefully acknowledged. DN acknowledges financial support from the Research Foundation -Flanders (FWO) through Grants 1SB9121N. R.V. acknowledges support by the Ministry of Education and Science of Ukraine (project No. 0121U110107).

* mgeilen@physik.uni-kl.de

- [1] A. A. Grachev, O. V. Matveev, M. Mruczkiewicz, M. A. Morozova, E. N. Beginin, S. E. Sheshukova, and A. V. Sadovnikov, *Applied Physics Letters* **118**, 10.1063/5.0051429 (2021).
- [2] A. Bukharaev, A. K. Zvezdin, A. P. Pyatakov, and Y. K. Fetisov, *Phys. Usp.* **61**, 1175– (2018).
- [3] Y. K. Fetisov and G. Srinivasan, *Applied Physics Letters* **88**, 143503 (2006).
- [4] A. V. Sadovnikov, A. A. Grachev, S. E. Sheshukova, Y. P. Sharaevskii, A. A. Serdobintsev, D. M. Mitin, and S. A. Nikitov, *Physical Review Letters* **120**, 257203 (2018).
- [5] C. Kittel, *Physical Review* **110**, 836 (1958).
- [6] H. Bömmel and K. Dransfeld, *Physical Review Letters* **3**, 83 (1959).
- [7] M. Pomerantz, *Physical Review Letters* **7**, 312 (1961).
- [8] E. Schlömann, *Journal of Applied Physics* **31**, 1647 (1960).

- [9] H. Matthews and F. R. Morgenthaler, *Physical Review Letters* **13**, 614 (1964).
- [10] P. Chowdhury, A. Jander, and P. Dhagat, *IEEE Magnetics Letters* **8**, 1 (2017).
- [11] N. I. Polzikova, S. G. Alekseev, I. I. Pyataikin, V. A. Luzanov, A. O. Raevskiy, and V. A. Kotov, *AIP Advances* **8**, 056128 (2018).
- [12] S. G. Alekseev, S. E. Dizhur, N. I. Polzikova, V. A. Luzanov, A. O. Raevskiy, A. P. Orlov, V. A. Kotov, and S. A. Nikitov, *Applied Physics Letters* **117**, 072408 (2020).
- [13] W. G. Yang and H. Schmidt, *Applied Physics Reviews* **8**, 10.1063/5.0042138 (2021).
- [14] M. Elhosni, O. Elmazria, S. Petit-Watelot, L. Bouvot, S. Zhgoon, A. Talbi, M. Hehn, K. A. Aissa, S. Hage-Ali, D. Lacour, F. Sarry, and O. Boumatar, *Sensors and Actuators A: Physical* **240**, 41 (2016).
- [15] L. Thevenard, I. S. Camara, S. Majrab, M. Bernard, P. Rovillain, A. Lemaître, C. Gourdon, and J.-Y. Duquesne, *Physical Review B* **93**, 134430 (2016).
- [16] N. K. P. Babu, A. Trzaskowska, P. Graczyk, G. Centała, S. Mieszczak, H. Głowiński, M. Zdunek, S. Mielcarek, and J. W. Klos, *Nano Letters* **21**, 946 (2021).
- [17] M. Küß, M. Heigl, L. Flacke, A. Hefele, A. Hörner, M. Weiler, M. Albrecht, and A. Wixforth, *Physical Review Applied* **15**, 1 (2021).
- [18] R. Verba, V. Tiberkevich, and A. Slavin, *Physical Review Applied* **12**, 054061 (2019).
- [19] P. J. Shah, D. A. Bas, I. Lisenkov, A. Matyushov, N. X. Sun, and M. R. Page, *Science Advances* **6**, 2 (2020).
- [20] P. Delsing, A. N. Cleland, M. J. Schuetz, J. Knörzer, G. Giedke, J. I. Cirac, K. Srinivasan, M. Wu, K. C. Balram, C. Bäuerle, T. Meunier, C. J. Ford, P. V. Santos, E. Cerda-Méndez, H. Wang, H. J. Krenner, E. D. Nysten, M. Weiß, G. R. Nash, L. Thevenard, C. Gourdon, P. Rovillain, M. Marangolo, J. Y. Duquesne, G. Fischerauer, W. Ruile, A. Reiner, B. Paschke, D. Denysenko, D. Volkmer, A. Wixforth, H. Bruus, M. Wiklund, J. Reboud, J. M. Cooper, Y. Q. Fu, M. S. Brugger, F. Rehfeldt, and C. Westerhausen, *Journal of Physics D: Applied Physics* **52**, 10.1088/1361-6463/ab1b04 (2019).
- [21] W. Han, X. Bu, M. Xu, al, Y. Li, J. Yang, and B. Jiang, *Journal of Physics D: Applied Physics* **52**, 153001 (2019).
- [22] M. Weiler, L. Dreher, C. Heeg, H. Huebl, R. Gross, M. S. Brandt, and S. T. B. Goennenwein, *Physical Review Letters* **106**, 117601 (2011).
- [23] Y. Yahagi, C. Berk, B. Hebler, S. Dhuey, S. Cabrini, M. Albrecht, and H. Schmidt, *Journal of Physics D: Applied Physics* **50**, 17LT01 (2017).
- [24] P. Kuszewski, J. Y. Duquesne, L. Becerra, A. Lemaître, S. Vincent, S. Majrab, F. Margaillan, C. Gourdon, and L. Thevenard, *Physical Review Applied* **10**, 1 (2018).
- [25] M. Küß, M. Heigl, L. Flacke, A. Hörner, M. Weiler, M. Albrecht, and A. Wixforth, *Physical Review Letters* **125**, 217203 (2020).
- [26] A. Mahmoud, F. Ciubotaru, F. Vanderveken, A. V. Chumak, S. Hamdioui, C. Adelman, and S. Cotofana, *Journal of Applied Physics* **128**, 161101 (2020).
- [27] P. Pirro, V. Vasyuchka, A. A. Serga, and B. Hillebrands, *Nature Reviews Materials* **6**, 1114 (2021).
- [28] P. Pirro, T. Sebastian, T. Brächer, A. A. Serga, T. Kubota, H. Naganuma, M. Oogane, Y. Ando, and B. Hillebrands, *Physical Review Letters* **113**, 1 (2014).
- [29] Q. Wang, A. Hamadeh, R. Verba, V. Lomakin, M. Mohseni, B. Hillebrands, A. V. Chumak, and P. Pirro, *npj Computational Materials* **6**, 192 (2020).
- [30] H. Schultheiss, K. Vogt, and B. Hillebrands, *Physical Review B* **86**, 054414 (2012).
- [31] P. Krivosik and C. E. Patton, *Physical Review B* **82**, 184428 (2010).
- [32] Á. Papp, W. Porod, and G. Csaba, *Nature Communications* **12**, 6422 (2021).
- [33] M. Kraimia, P. Kuszewski, J.-Y. Duquesne, A. Lemaître, F. Margaillan, C. Gourdon, and L. Thevenard, *Physical Review B* **101**, 144425 (2020).
- [34] I. Lisenkov, A. Jander, and P. Dhagat, *Physical Review B* **99**, 184433 (2019).
- [35] X. Zhang, G. E. Bauer, and T. Yu, *Physical Review Letters* **125**, 077203 (2020).
- [36] M. Geilen, F. Kohl, A. Nicoloiu, A. Müller, B. Hillebrands, and P. Pirro, *Applied Physics Letters* **117**, 213501 (2020).
- [37] T. Sebastian, K. Schultheiss, B. Obry, B. Hillebrands, and H. Schultheiss, *Frontiers in Physics* **3**, 1 (2015).
- [38] F. Kargar and A. A. Balandin, *Nature Photonics* **15**, 10.1038/s41566-021-00836-5 (2021).
- [39] M. Geilen, A. Nicoloiu, D. Narducci, M. Mohseni, M. Bechberger, M. Ender, F. Ciubotaru, A. Müller, B. Hillebrands, C. Adelman, and P. Pirro, Fully resonant magneto-elastic spin-wave excitation by surface acoustic waves under conservation of energy and linear momentum (2021), arXiv:2106.14705 [cond-mat.other].
- [40] C. Kittel, *Review of modern physics* **21**, 745 (1949).
- [41] A. Gurevich and G. A. Melkov, *The Journal of dermatologic surgery and oncology* (CRC Press, 1996).
- [42] D. D. Stancil and A. Prabhakar, *Spin Waves: Theory and Applications* (2009) p. 364.
- [43] A. P. Mayer, *Ultrasonics* **48**, 478 (2008).
- [44] A. P. Mayer, *Physics Reports* **256**, 237 (1995).
- [45] A. Vansteenkiste, J. Leliaert, M. Dvornik, M. Helsen, F. Garcia-Sanchez, and B. Van Waeyenberge, *AIP Advances* **4**, 107133 (2014).
- [46] aithericon.com.
- [47] Supplement material.
- [48] T. Brächer, P. Pirro, and B. Hillebrands, *Physics Reports* **699**, 1 (2017).
- [49] R. Verba, M. Carpentieri, G. Finocchio, V. Tiberkevich, and A. Slavin, *Physical Review Applied* **7**, 064023 (2017).

Supplement Material: Parametric Excitation and Instabilities of Spin Waves driven by Surface Acoustic Waves

Moritz Geilen,¹ Roman Verba,² Alexandra Nicoloiu,³ Daniele Narducci,^{4,5} Adrian Dinescu,³ Milan Ender,¹ Morteza Mohseni,¹ Florin Ciubotaru,⁴ Mathias Weiler,¹ Alexandru Müller,³ Burkard Hillebrands,¹ Christoph Adelmann,⁴ and Philipp Pirro¹

¹Fachbereich Physik and Landesforschungszentrum OPTIMAS, Technische Universität Kaiserslautern, Germany*

²Institute of Magnetism, Kyiv 03142, Ukraine

³National Institute for Research and Development in Microtechnologies, Bucharest R-07719, Romania

⁴imec, Leuven B-3001, Belgium

⁵KU Leuven, Departement Materiaalkunde, 3001 Leuven, Belgium

(Dated: January 12, 2022)

TIME-RESOLVED MEASUREMENT

Here, we prove that the instability processes are indeed generated by the SAW and not caused by electromagnetic leakage. Therefore, time-resolved μ BLS measurements have been performed. SAW pulses with a pulse duration of $\tau = 100$ ns and an RF-power of +30 dBm were excited and tracked along their propagation. In the upper panel of Fig. 1, the extracted BLS intensity around f_0 is displayed, while in the lower one, the integrated signal of f_1 and f_2 is shown. Due to some residual BLS signal from the SAW, the first is visible throughout the whole distance, while the signal produced by the instability process only appears on the magnetic material. Despite the exponential decay of the SAW, the amplitude of the magneto-elastic field is large enough to overcome the instability threshold until the end of the magnetic rectangle. The temporal coincidence of the two signals prove that the instability processes are driven by the magneto-elastic field and not by electromagnetic leakage, which would be much faster and appear instantly over the whole distance.

MICROMAGNETIC SIMULATION

In the following, the details for the micromagnetic simulations will be presented. For the simulated magnetic pads has an edge length of $70 \mu\text{m} \times 70 \mu\text{m} \times 18 \text{nm}$ and was divided into $1024 \times 1024 \times 1$ cells. In addition, periodic boundary conditions were assumed. The width of the SAW beam is $50 \mu\text{m}$. The following parameters have been used: saturation magnetization $M_S = 950 \text{ kA/m}$, exchange stiffness $A_{ex} = 15 \text{ pJ/m}$, Gilbert damping parameter $\alpha = 0.0043$ and the magnetoelastic coupling constants $B_1 = B_2 = -8.8 \text{ MJ/m}^3$ [?]. Further an uniaxial anisotropy along the x-axis has been assumed with $K_{u1} = 1600 \text{ J/m}^3$ [?]. The angle between the x-axis and the external magnetic field is $\varphi = 45^\circ$. The surface acoustic wave has been implemented as two plain waves of the strain components S_{xx} and S_{xz} which are in phase quadrature:

$$\begin{aligned} S_{xx} &= A \sin(2\pi(x/\lambda_R - ft)) \\ S_{xz} &= A \cos(2\pi(x/\lambda_R - ft)) \\ S_{yy} &= S_{xy} = S_{zz} = S_{yz} = 0. \end{aligned} \quad (1)$$

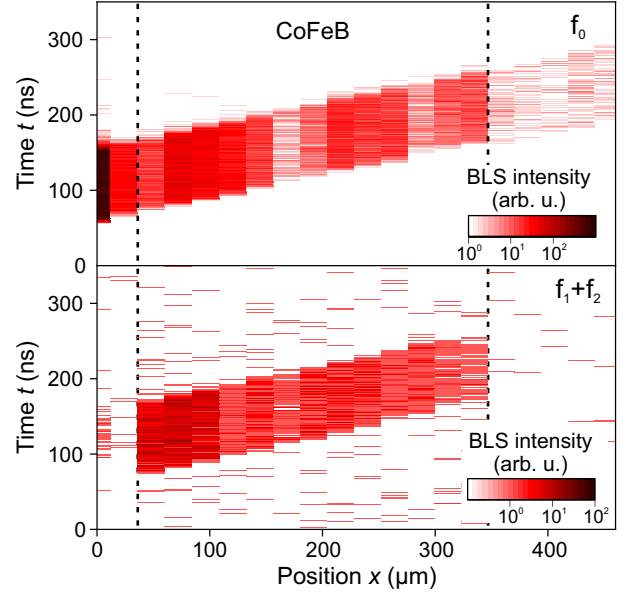


FIG. 1: Time-resolved μ BLS measurement along the propagation direction of the SAW at a applied field of 2 mT. The upper panel shows the intensity for f_0 , while the lower panel shows the integrated signal for the modes f_1 and f_2 .

The wave vector was set by the wavelength $k_R = \frac{2\pi}{\lambda_R}$ with $\lambda_R = 682 \text{ nm}$. Further, a thermal field corresponding to the temperature $T = 300 \text{ K}$ has been used in order to account for the thermal occupation of the magnon modes.

Figure 2 a shows the spectra obtained from the micromagnetic simulation for an external field of $\mu_0 H_{\text{ext}} = 2 \text{ mT}$. For a strain amplitude of $A = 10 \times 10^{-6}$ the spin wave spectrum is dominated by the thermal spin waves. Only a minor linear excitation can be seen at f_0 . For the nonlinear case with a strain amplitude of $A = 50 \times 10^{-6}$ secondary modes appear. The intensity of the pumped modes f_1 and f_2 exceeds that of the initial mode f_0 .

FFT Intensity extracted for the frequencies of the initial and secondary modes is shown in Fig. 2 b. The confluence process $f_3 = f_0 + f_1$ and $f_4 = f_0 + f_2$ fulfill both energy and momentum conservation.

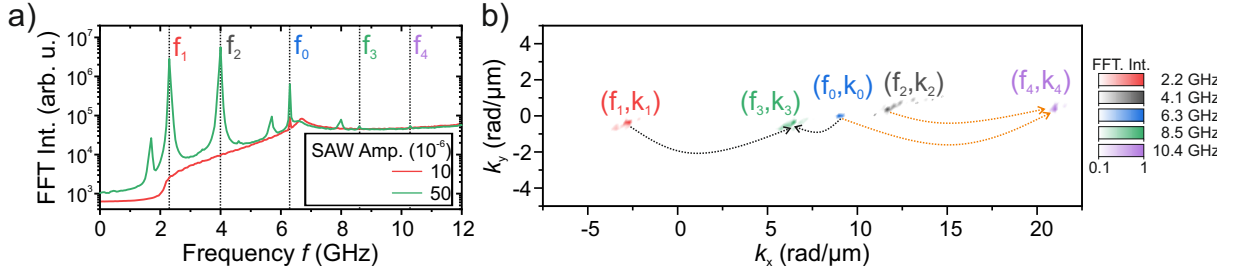


FIG. 2: a) The FFT intensity as a function of the frequency extracted from the micromagnetic simulation for $\mu_0 H_{\text{ext}} = 2$ mT. The linear case is shown in red and the nonlinear in green. b) Extracted FFT. intensity for all secondary modes involved in the confluence process leading to f_3 and f_4

ANALYTICAL ANALYSIS OF SAW-DRIVEN SPIN-WAVE INSTABILITIES

The spin-wave dispersion in an in-plane magnetized film accounting for an uniaxial anisotropy in x -direction is given by:

$$\omega_k^2 = \Omega_{\text{IP}} \Omega_{zz} = (\omega_H + \omega_M \lambda^2 k^2 + \omega_M F_{y'y'}) \times (\omega_H + \omega_M \lambda^2 k^2 + \omega_M (1 - f(kh))), \quad (2)$$

with

$$F_{y'y'} = \frac{k_{\perp}^2}{k^2} f(kh) - \frac{B_a}{\mu_0 M_s} \sin^2 \phi_M, \quad (3)$$

$f(x) = 1 - (1 - e^{-|x|})/|x|$ is “thin film function”, $k_{\perp} = k_y \cos \phi_M - k_x \sin \phi_M$ is the perpendicular to the static magnetization component of spin-wave wave vector, and $B_a = 2K_u/M_s$ is the anisotropy field. All the used parameters are the same as in the micromagnetic simulations.

A theory of parametric interaction of spin wave (SW) with acoustic pumping was developed in [?]. Dynamic equations for SW amplitudes $c_{\mathbf{k}}$ read:

$$\frac{dc_{\mathbf{1}}}{dt} + i\omega_{\mathbf{1}}c_{\mathbf{1}} + \Gamma_{\mathbf{1}}c_{\mathbf{1}} = i\gamma_{0,12}q_{\text{SAW}}c_{\mathbf{2}}^*, \quad (4)$$

where q_{SAW} is the SAW amplitude, with the short notations $c_{\mathbf{1}} \equiv c_{\mathbf{k}_1}$. The SW and SAW wave vectors satisfy the relation $\mathbf{k}_0 = \mathbf{k}_1 + \mathbf{k}_2$, and the parametric coupling efficiency is given by:

$$\gamma_{0,12} = \frac{\gamma B_1}{M_S} \bar{S}_{0,xx} (m_{1,x}^* m_{2,x}^* - \mathbf{m}_1^* \cdot \mathbf{m}_2^* \cos^2(\phi_M)). \quad (5)$$

Here $\bar{S}_{0,xx}$ is the thickness average of SAW strain $S_{0,xx}$ (physical strain is related to SAW amplitude as $S_{ij}(\mathbf{r}, t) = q_0(t)S_{0,ij}(z)\exp(ik_0x) + \text{c.c.}$). $\mathbf{m}_{\mathbf{k}} = [-m_{\text{IP}} \sin(\phi_M), m_{\text{IP}} \cos(\phi_M), m_z]$ is the SW mode structure with $m_{\text{IP}} = \sqrt{\Omega_{zz}/2\omega_k}$ and $m_z = i\sqrt{\Omega_{\text{IP}}/2\omega_k}$ (with this SW structure selection SW norm is equal to 1). For brevity we disregard effect of the off-diagonal SAW strain $S_{xz} = S_{zx}$, in the considered case this strain component, averaged over the ferromagnetic layer, is more than 10 times

smaller than the diagonal strain. Also analysis shows that off-diagonal contribution does not lead to any qualitatively new features. The SW profile across the ferromagnet thickness is assumed to be uniform. In Eq. 5 one can point two contributions to the parametric coupling – the second is proportional to SW ellipticity, like in standard microwave parallel pumping, while the first one, defined by square of dynamic magnetization component, appears only in the case of anisotropy-type pumping, which is realized, e.g., for magneto-elastic [?] or magneto-electric [?] drive. The threshold of SAW-SW three-wave splitting in a general case of a non-resonant process is equal to: [?]

$$q_{\text{th}} = \frac{1}{|\gamma_{0,12}|} \sqrt{\Gamma_1 \Gamma_2 \left(1 + \frac{\delta\omega^2}{(\Gamma_1 + \Gamma_2)^2}\right)}, \quad (6)$$

where $\delta\omega = \omega_{\text{SAW}} - (\omega_1 + \omega_2)$ is the detuning from three-wave resonance splitting condition. The values for the threshold of this acoustic pumping process are shown in fig.3. Small thresholds, naturally, correspond to resonance condition ($\omega_{\text{SAW}} = \omega_1 + \omega_2$), at which, however, the dependence of threshold is also quite pronounced. The minimal calculated threshold ($q_{\text{th,min}}^{\text{SAW-SW}} = 7.4 \times 10^{-5}$) corresponds to the splitting into SWs with $\mathbf{k}_1 = (8.1, -0.5)$ rad/ μm and $\mathbf{k}_2 = (1.2, 0.5)$ rad/ μm (see. Fig. 3 diamonds).

The second possible mechanism that leads to the population of the SW modes **1** and **2** is the three-magnon splitting of non-resonantly excited SW at $\{f_{\text{SAW}}, k_{\text{SAW}}\}$. Expression for the splitting threshold is the same as Eq. (6), where threshold SAW amplitude q_{th} is changed to SW amplitude c_0 , and the coefficient $\gamma_{0,12}$ to three-magnon scattering coefficient $V_{0,12}$. The last one is straightforwardly calculated using the Hamiltonian formalism [? ?]. An explicit expression is rather cumbersome and is not presented here. The relation of SW amplitude c_0 with SAW amplitude is given by:

$$c_0 = \frac{i\gamma b_0 q_0}{i(\omega_0 - \omega_{\text{SAW}}) + \Gamma_0} \quad (7)$$

with the linear coupling efficiency

$$b_{\mathbf{k}} = \frac{2B_1}{M_S} m_{\mathbf{k},x}^* \bar{S}_{\mathbf{k},xx} \cos \phi_M. \quad (8)$$

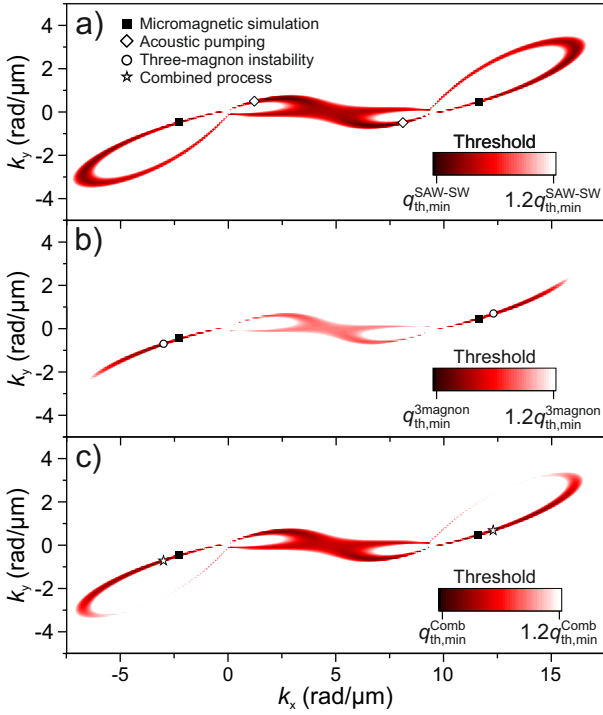


FIG. 3: Calculated threshold for a) the direct SAW-SW process of acoustic pumping process, b) the first order spin wave instability of non-resonantly excited SW, c) the combined process of direct SAW-SW and three-magnon splitting. The spin-wave modes with minimal threshold for the direct SAW-SW process $q_{th,min}^{SAW-SW}$ (diamond), the first order spin wave instability of non-resonantly excited SW (Circle) and the combined process $q_{th,min}^{Comb}$ (Star) are indicated. The position of those modes extracted from the micromagnetic simulations is shown by the black squares.

The minimal threshold for this three-magnon process is observed for different secondary SWs: $\mathbf{k}_1 = (12.3, 0.1) \text{ rad}/\mu\text{m}$, $\mathbf{k}_2 = (-3.0, -0.1) \text{ rad}/\mu\text{m}$. But, it is significantly (64%) larger than for SAW-SW splitting, $q_{th,min}^{3magnon} = 1.21 \times 10^{-4}$.

Taking the three-magnon splitting additionally into account for the calculation of threshold for the acoustic pumping, the new minimal threshold of the combined process

($q_{th,min}^{Comb} = 6.3 \times 10^{-5}$) is reached at $\mathbf{k}_1 = (-3, -0.7) \text{ rad}/\mu\text{m}$, $\mathbf{k}_2 = (12.3, 0.7) \text{ rad}/\mu\text{m}$ (see Fig. 3 circle). The calculated threshold for the wave vectors obtained by micromagnetic simulations is $q_{th,Simulation}^{Comb} = 6.67 \times 10^{-5}$. The position of those modes is indicated by the black squares in Fig. 3.

Concerning the generation of the higher frequency modes f_3 and f_4 it has to be mentioned that the three-wave process includes both the SAW-SW confluence as well as three-magnon confluence. An important observation is that the states at **3** and **4** are not linear eigenmodes of the spin-wave system. This implies that they cannot be a result of a spontaneous splitting process. Although non-resonant splitting is possible, both split states need to be non-resonant. The situation when one split state is in the resonance ($f_{1,2}$ in our case), while the other one is non-resonant, is impossible [?]. Therefore, the four-wave process has to be stimulated by the spin waves at $f_{1,2}$.

In order to compare the magnitude of three-wave and four-wave terms a Hamiltonian approach was used. In the dynamical equations these terms appear as

$$\frac{dc_3}{dt} \sim \mathcal{V}_{3,01}^* q_0 c_1 + V_{3,01}^* c_0 c_1 + \frac{1}{2} W_{00,23} c_0^2 c_2, \quad (9)$$

where $W_{ij,kl}$ is the four-magnon coefficient and $\mathcal{V}_{3,01}$ is the three-wave coefficient of the SAW+SW \rightarrow SW process. In fact, one needs to compare the values of $\mathcal{V}_{3,01}(dc_0/dq_0)$, $V_{3,01}^*$ and $\frac{1}{2} W_{00,23} c_0$. Calculations made using the Hamiltonian formalism gives $V \sim 2\pi \times 9 \text{ GHz}$ and $W \sim (25 - 75) \text{ GHz}$ for the different processes. Using a SAW-SW perturbation approach we get $\mathcal{V}(dc/dq) \sim 2\pi \times 17 \text{ GHz}$. The values of the directly excited mode amplitude is known from the threshold of the first three-wave splitting process, $c_0 \approx 0.0045$. Thus, in all the studied range (one order of magnitude above the threshold value) the four-magnon process is much weaker (two orders of magnitude) than the three-magnon one. In addition, it can be concluded that the SAW-SW confluence process is two times more efficient than the three-magnon confluence process, but, since confluence processes are non-threshold, both these processes contributes to the appearance of signals at $f_{3,4}$.